UDK 549.521.4:52-334.2
Original scientific article/Izvirni znanstveni članek

ISSN 1580-2949
Mater. Tehnol.

MECHANICAL AND MICROSTRUCTURAL BEHAVIOUR OF STIR-CAST AA7065–B4C–GRAPHITE HYBRID COMPOSITES WITH OPTIMIZED REINFORCEMENT CONTENT

MEHANSKE IN MIKROSTRUKTURNE LASTNOSTI HIBRIDNEGA KOMPOZITA AA7065-B4C Z OPTIMIZIRANO VSEBNOSTJO OJAČITVE, IZDELANEGA S POSTOPKOM NJENEGA UMEŠAVANJA V TALINO

Madhan Arumugam Baladhandapani*, **Parthiban Alagesan**
Department of Mechanical Engineering, Vels Institute of Science, Technology & Advanced Studies (VISTAS), Tamil Nadu, India

Prejem rokopisa – received: 2025-12-06; sprejem za objavo – accepted for publication: 2026-03-15

doi:10.17222/mit.2025.1626

High-strength aluminium hybrids reinforced with ceramics and solid lubricants are used in structural and tribological parts. AA7065 supports precipitation hardening and the incorporation of B_4C and graphite. Quantitative links between reinforcement content and mechanical behaviour remain limited for AA7065. This study quantifies the effect of B_4C content at a near-constant graphite level on hardness, tensile metrics, and Izod impact energy. Hybrids containing 0–7 *w*/% B_4C with 3 *w*/% graphite were produced by vortex-assisted stir casting, T6-treated, machined into ASTM E8 and ASTM D256 specimens, tested, and characterized using optical/SEM microscopy, followed by ANOVA response-surface analysis. Strengthening is evident, with hardness increasing from about 100 HV to about 130 HV (30 %), and tensile strength increasing from about 300 MPa to about 360 MPa (20 %) at 7 *w*/% B_4C. Damage tolerance declined, with elongation decreasing from about 12 % to about 5 %, and Izod impact energy decreasing from about 20 J to about 12 J. The pattern is consistent with load transfer and dislocation blocking combined with particle-assisted void nucleation. These data guide reinforcement selection for AA7065–B_4C–graphite composites used in high-strength parts with controlled deformability. Future work will target fatigue and wear response under service loading and evaluate graphite fraction and particle size as design variables.

Keywords: stir casting, AA7065, boron carbide (B4C), graphite, mechanical properties

Hibridi na osnovi aluminija z visoko trdnostjo, ojačani s keramiko in trdnimi mazivi, se uporabljajo v konstrukcijskih komponentah in delih, ki so izpostavljeni močni obrabi. Zlitina na osnovi aluminija tipa AA7065 omogoča izločevalno (disperzijsko) utrjevanje ter vgraditev (vkomponiranje) B_4C in grafita. Vendar so količine ojačitve dodane v talino zlitine AA7065 omejene glede na optimalne oziroma želene mehanske lastnosti. V tem članku avtorji predstavljajo študijo vpliva vsebnosti B_4C pri skoraj konstantni vsebnosti grafita na trdoto, natezno trdnost in Izodovo udarno žilavost. Izdelani hibridi so vsebovali od 0 do 7 *w*/% B_4C in 3 *w*/% grafita. Izdelani so bili s postopkom umešavanjem finih delcev karbida in grafita v talino z vrtinčnim premešavanjem taline. Po litju vzorcev v kokile in njihovem ohlajanju so bili le ti toplotno obdelani s postopkom T6, strojno obdelani v natezne preizkušance po standardu ASTM E8 in žilavostne preizkušance za določitev udarne žilavosti (energije loma) na Izodovem nihalu po standardu ASTM D256. Prelomi preizkušancve so bili optično pregledani in okarakterizirani s svetlobnim in elektronskim mikroskopom z analizo odziva površine ANOVA. Ojačitev je bila očitna; pri dodatku 7 *w*/% B_4C se je trdota povečala s približno 100 HV na približno 130 HV (30 %) in natezna trdnost se je povečala s približno 300 MPa na približno 360 MPa (20 %). Toleranca do poškodb se je zmanjšala; raztezek se je zmanjšal s približno 12 % na približno 5 %, Izodova udarna energija pa se je zmanjšala s približno 20 J na približno 12 J. Mehanizem loma vzorcev hibrida poteka s prenosom obremenitve in blokiranjem dislokacij v kombinaciji z nukleacijo praznin s pomočjo delcev. Izvedena raziskava omogoča določitev optimalne vsebnosti izbrane ojačitve za kompozite AA7065–B_4C–grafit, ki se uporabljajo v visokotrdnostnih komponentah z nadzorovano deformabilnostjo. Avtorji v prihodnosti načrtujejo še raziskave usmerjene v analizo utrujanja materiala in tribološke lastnosti teh materialov glede na količino dodanega grafita in velikosti karbidnih delcev.

Ključne besede: umešavanje delcev ojačitve v talino s postopkom vrtilnega omešavanja, aluminijeva zlitina tipa AA7065, borov karbid (B_4C), grafit, mehanske lastnosti

1 INTRODUCTION

Advanced aluminium alloys are central to modern transportation, defence, and energy systems because they combine low density with high specific strength, good corrosion resistance, and attractive recyclability within a relatively mature manufacturing infrastructure. Within this, Al–Zn–Mg–Cu alloys occupy an important position for aerospace and high-performance structural applications, since controlled precipitation of the η and η' phases in a heat-treated matrix provides high yield strength and good fatigue resistance while retaining acceptable fracture toughness.[1] At the same time, metal-matrix composites based on aluminium, reinforced with ceramic particles and solid lubricants, are gaining attention as candidate materials for components that experience abrasive wear, impact loading, and complex stress states in service. Hybrid metal-matrix composites that incorporate a hard ceramic phase, such as boron carbide (B_4C), together with a soft solid lubricant, such as graph-

---

*Corresponding author's e-mail:
madhanbaladhandapani@gmail.com (Madhan A. Baladhandapani)

ite, are particularly good because they provide high stiffness and strength from the ceramic reinforcement while also improving seizure resistance and reducing friction in dry sliding conditions. Among the various fabrication routes, liquid metallurgy techniques, such as stir casting, remain industrially relevant since they are relatively economical, compatible with conventional foundry practice, and capable of producing near-net-shape components without elaborate equipment.[2]

The performance of such composites is intimately linked to the quality of particle incorporation during casting, the subsequent heat-treatment schedule, and the detailed morphology of the reinforcement–matrix interface, which together control load transfer, dislocation behaviour, and damage initiation under service loads.[3] Considerable effort has therefore been directed towards tailoring microstructures through alloy design, solid-state processing, and advanced thermo-mechanical treatments so that aluminium alloys and their composites can satisfy stringent weight and durability constraints imposed by modern engineering design. Previous research on aluminium-based composites reinforced with ceramics such as SiC, Al_2O_3, TiC, and B_4C reported significant gains in hardness, tensile strength, and wear resistance when the particle distribution was uniform, and the interfacial bonding was strong. Separate work on graphite- or MoS_2-containing aluminium and magnesium alloys showed that the inclusion of a solid lubricant phase could reduce friction and improve seizure resistance in sliding contact, especially when the lubricant was finely dispersed within the matrix.[4] Studies on hybrid metal–matrix systems that combined hard and lubricating phases suggested that an appropriate balance of reinforcements could enhance dry sliding behaviour without unacceptable reduction in static strength.

Cheng et al. (2026) used RSM and random forest to link drilling parameters to micro-hole quality metrics in Inconel 718.[11] Ma et al. (2025) examined how aging changes microstructure and mechanical response in additively manufactured FeCoCrMnNi HEA composites.[12] Meng et al. (2025/2026) studied in-situ rolling friction stir welding and linked microstructural modification to stress-corrosion mechanisms.[13] Peng et al. (2025) simulated laser welding of 6056 Al T-joints and optimized key parameters using orthogonal testing.[14] Qiao et al. (2024) monitored in situ AFSD of AA6061 and quantified how rotation speed alters the microstructure and mechanical anisotropy.[15] Yuan et al. (2025) built a 3D non-uniform line-contact EHL model for harmonic drives. They used it to optimize spatial modification parameters to improve lubrication behavior.[16] Zheng et al. (2026) predicted friction and wear of copper-free brake materials using a PSO-FPA-optimized BP neural network.[17] The field is moving toward quantitative, optimization-centered materials engineering. It combines controlled experiments, statistical design, and fast predictive models. Hybrid approaches also integrate physical or mechanistic descriptors to keep predictions usable, not just accurate (**Table 1**). This direction supports the current composite study by motivating a tighter link between reinforcement content, processing choices, and mechanical-property trade-offs, and by using transparent optimization logic rather than trial-and-error.

Researchers also investigated the influence of particle size, weight fraction, and casting conditions on porosity, clustering, and wetting, and emphasised the need for optimised stirring parameters and preheating protocols to minimise interfacial reactions and gas entrapment during melt processing. Beyond microstructural characterisation, several studies applied statistical design of experiments, response surface methodology, and artificial intelligence tools to model the influence of process parameters on the mechanical and tribological performance of aluminium composites produced by casting, friction stir processing, or additive manufacturing. These approaches demonstrated that data-driven models could

Table 1: Modelling, optimization, and property-microstructure links relevant to composite design

Reference/ citation	Methodology/approach	Materials/parameters studied	Key findings/results	Relevance to current study
Ren et al., 2025	Dual-output DL + physics constraints, partitioning + properties	Metallic datasets, microstructure descriptors, stress–strain targets	Δinterpretability, Δaccuracy, Δcomputational efficiency	Supports hybrid modelling for composition-property mapping.[5]
Wang et al., 2022	MD-informed ML + high-throughput optimization	Laser parameters, Ni-based single-crystal superalloy	Δefficiency, ∇recast layer, ∇taper	Shows a data-efficient optimization workflow.[6]
Zhang et al., 2022	ML predictor + multi-objective genetic algorithm	Taper, recast layer, drilling efficiency metrics	∇taper, ∇recast layer, Δefficiency	Multi-objective optimization template.[7]
Xu et al., 2025	Gravity + friction compensation, control strategy validation	Normal force, friction, positioning error	Δpositioning accuracy, ∇slip risk	Useful for robust process-control framing.[8]
Zheng et al., 2025	Experiments vs mesh size/content, tribology tests	Andalusite content, mesh, friction/wear temperatures	Δheat-fade resistance, Δhardness, Δfriction stability	Reinforcement-content effects on performance trade-offs.[9]
Xiao et al., 2024	Multilayer heterogeneous architecture design	Layered pyrocarbon composite architecture	Δstrength, Δtoughness	Microstructure design for strength-toughness synergy.[10]

Table 2: Material conditions used for the principal comparison series and modelling inputs

Condition ID	Matrix	B_4C (*w*/%)	Graphite (*w*/%)	Notes used in analysis workflow
M0	AA7065	0	0	Baseline reference for ΔX (%) calculations
H4G3	AA7065	4	3	Reinforced condition used for mechanical and microstructural comparisons
H7G3	AA7065	7	3	Reinforced condition used for mechanical and microstructural comparisons
RSM	AA7065	Variable	Variable	Composition variables *A* (B_4C) and *B* (graphite) used in polynomial modelling

capture the influence of reinforcement content and processing variables on material properties, and they provided possible approaches for virtual optimization of alloy-composite systems.[18]

While several investigations addressed wrought and cast series alloys reinforced with different ceramics, systematic work on AA7065, a high-strength aerospace alloy, remained limited despite its favourable hardening response and potential for hybrid reinforcement. The available literature on AA7065 has mainly focused on precipitation behaviour, welding, and corrosion aspects of the monolithic alloy, with comparatively fewer studies on particle-reinforced variants or hybrid composites.[19] Only a limited number of reports examined B_4C- or graphite-reinforced alloys, and these studies often used different base alloys, reinforcement levels, matrix tempers, and testing protocols, making direct comparisons difficult. As a result, the current understanding of the relationships among B_4C content, graphite content, and mechanical performance in AA7065-based hybrid composites remains incomplete, particularly under quasi-static tensile and impact loading relevant to structural design. In addition, most earlier works relied on qualitative assessment of fracture surfaces and simple property comparisons, without developing compact predictive equations that relate reinforcement content to tensile strength, yield strength, and hardness within a defined compositional window.[20]

Limited attention was given to the concurrent influence of hard ceramic and solid-lubricant phases on the micro-mechanisms of fracture, such as void nucleation at particle–matrix interfaces, particle cracking, crack deflection through graphite-rich regions, and dimple formation in the aluminium ligaments.[21] There was also a lack of quantitative optimization studies that integrated experimental data with statistical models to identify reinforcement combinations that align with engineering targets for stiffness, strength, and impact energy in a given alloy system. These gaps implied that engineers seeking to design components from AA7065-based hybrid composites lacked robust guidelines for selecting reinforcement levels that satisfy both structural and tribological requirements, especially when using stir casting and conventional T6 heat treatments in the manufacturing route.[22]

The novelty of the present work arises from the focused investigation of AA7065–B_4C–graphite hybrid metal–matrix composites fabricated by vortex-assisted stir casting followed by T6 heat treatment, combined with systematic mechanical testing, microstructural and fractographic characterization, and regression-based analysis of variance to derive explicit relationships between reinforcement content and mechanical properties.[23] By examining tensile, hardness, and impact responses for composites containing different B_4C levels at nearly constant graphite content, and by coupling these measurements with direct observations of particle distribution and fracture morphology, the study offers a coherent framework that links processing, microstructure, and mechanical behaviour in a relevant alloy system.[24]

The objective of the present work is to investigate the mechanical and microstructural behaviour of stir-cast AA7065–B_4C–graphite hybrid metal–matrix composites and to establish quantitative relationships between B_4C and graphite contents as well as the resulting hardness, tensile strength, yield strength, and impact energy so that suitable reinforcement combinations can be identified for structural applications.

2 MATERIALS AND METHODS

AA7065 aluminium alloy ingots were selected as the matrix feedstock and were sectioned into charges suitable for crucible melting. Boron carbide (B_4C) powder and graphite powder were used as reinforcements, and composition sets were defined by mass fraction prior to melting. A base-alloy condition and hybrid-composite conditions were prepared, and the nominal reinforcement contents used for the principal comparison series are listed in **Table 2**.

Powder masses were weighed using an analytical balance, and batch identities were preserved during casting, heat treatment, machining, and testing. Reinforcement powders were preheated at 400 °C for 45 min to reduce thermal gradients during addition and to limit moisture-related gas pickup. Alloy charges were melted in a graphite crucible in an electric-resistance furnace, and the melt temperature was stabilised at 750 °C before any additions were introduced. Dissolved-gas removal was carried out using hexachloroethane tablets, and surface slag was removed before stirring to reduce oxide entrainment during vortex formation. A schematic of the casting arrangement is shown in **Figure 1**, and the fabrication sequence used for all batches is shown in **Figure 2**.

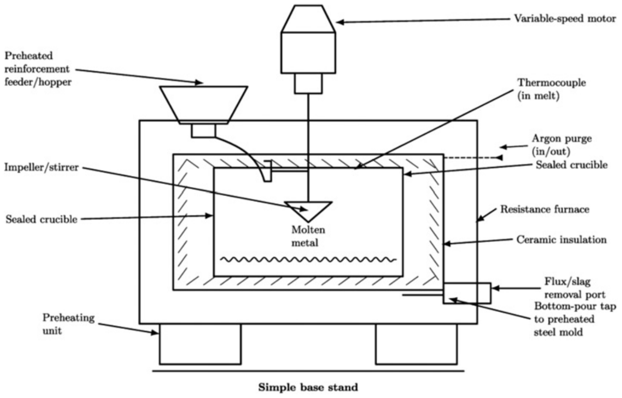

Figure 1: Schematic of the stir-casting setup

Vortex-assisted stir casting was performed by inserting an impeller into the melt after temperature stabilization and by applying mechanical stirring at 500 min^{-1}. Preheated B_4C and graphite were added into the established vortex over 3–4 min, and stirring was continued for 8 min after the completion of powder feeding to promote dispersion and to limit clustering. The impeller immersion depth was held constant across batches, and the melt temperature was controlled at the casting setpoint during stirring and before pouring. The composite slurry was discharged through a bottom-pour outlet into steel moulds preheated to 250 °C, with a nominal casting cross-section of (25 × 25) mm. All processing parameters associated with melting, degassing, vortex stirring, powder feeding time, post-addition stirring time, and mould preheating are listed in **Table 3**. Cast bars were cooled to room temperature, removed from the moulds, and identified by batch before heat treatment.

Table 3: Stir-casting and mould parameters used for all batches

Parameter	Value
Melt temperature	750 °C
Reinforcement preheating	400 °C, 45 min
Degassing agent	Hexachloroethane tablets
Stirring speed	500 min^{-1}
Powder feeding time	3–4 min
Post-feeding stirring time	8 min
aspnumMould preheat temperature	250 °C
Casting cross-section	(25 × 25) mm
Casting route	Bottom-pour into steel mould

A T6 heat-treatment cycle was applied to all cast bars to standardise precipitation strengthening. Solution treatment was conducted at 480 °C for 2 h, followed by water quenching to room temperature to retain a supersaturated solid solution. Artificial ageing was performed at 120 °C for 24 h to develop strengthening precipitates in AA7xxx systems. The time–temperature schedule used for solution treatment, quenching, and ageing is listed in **Table 4**, and the same cycle was applied to each batch to limit thermal-history effects on mechanical response.

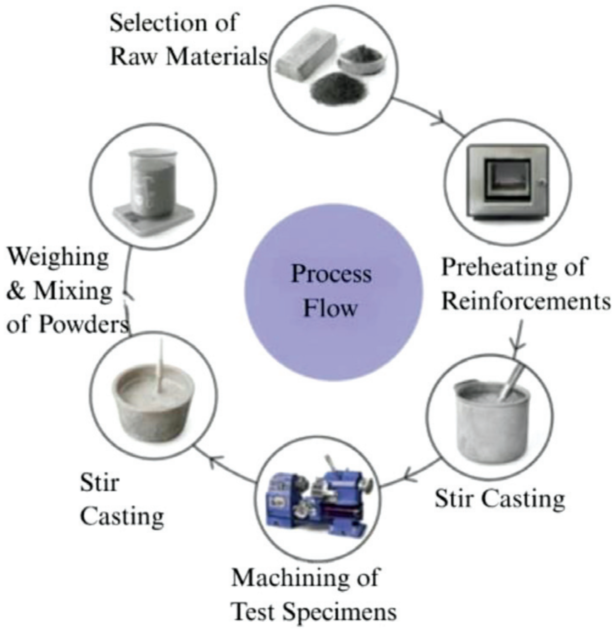

Figure 2: Process flowchart for the composite fabrication

Table 4: T6 heat-treatment schedule applied under all conditions

Step	Temperature	Time	Quench/ambient step
Solution treatment	480 °C	2 h	Water is quenched to room temperature
Artificial ageing	120 °C	24 h	Air cools to room temperature

Mechanical-test specimens were machined from the heat-treated bars in accordance with ASTM standards. The tensile specimen geometry followed ASTM E8 sub-size flat requirements, and the impact specimen geometry followed ASTM D256 Izod requirements. The corresponding geometrical definitions are shown in **Figure 3** and **Table 5**. Tensile testing was performed on a universal testing machine with a 100 kN load frame and a calibrated load cell for force acquisition. An extensometer with a 25 mm gauge length was attached to the reduced section, and loading was applied at a crosshead speed of 1 mm min^{-1} until fracture. For each tensile specimen, force-extension and force-strain data were recorded continuously, and engineering stress and engineering strain were computed from the raw signals using standard definitions. Engineering stress, σ_e, was calculated from the recorded force, F, and the initial cross-sectional area, A_0, using $\sigma_e = F/A_0$. Engineering strain, ε_e, was computed from extensometer extension, ΔL, and the initial gauge length, L_0, using $\varepsilon_e = \Delta L/L_0$. Yield strength was determined using the 0.2 % offset method, defined by the intersection of the measured σ_e (ε_e) curve with a line having slope equal to the initial elastic modulus, E, and shifted by an offset strain of 0.002, expressed as $\sigma = E(\varepsilon_e - 0.002)$. Ultimate tensile strength, σUTS, was taken as the maximum recorded engineering stress, σUTS = max(σ_e). Elongation to fracture was computed

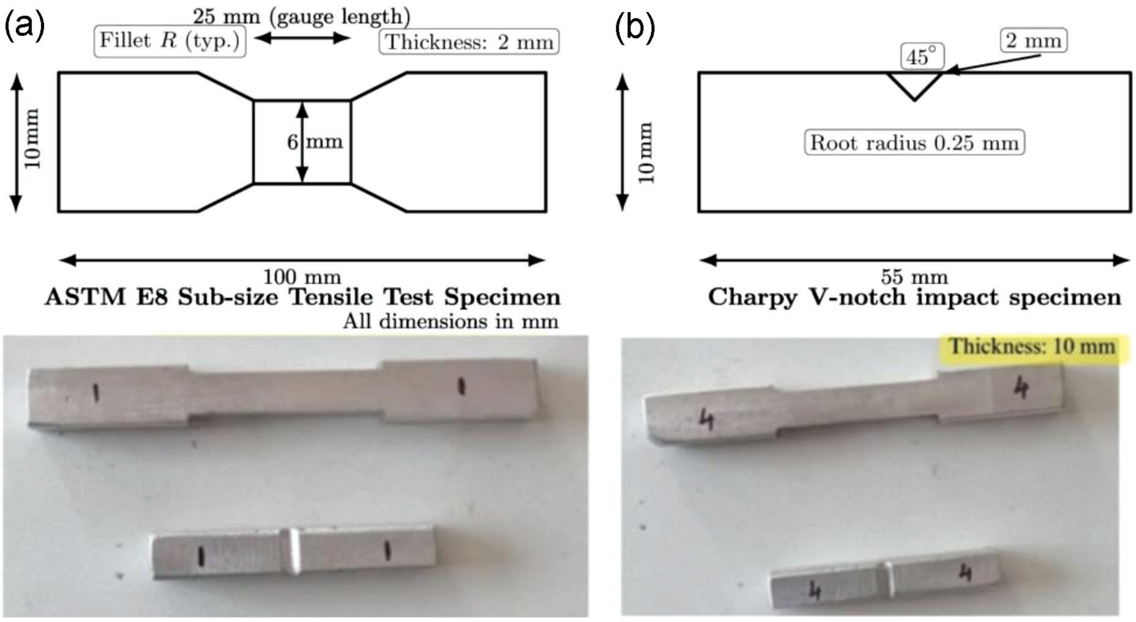

Figure 3: a) ASTM E8 subsize tensile specimen before and after fracture; b) V-notched impact specimen before and after fracture

Table 5: Mechanical testing standards, specimen dimensions, acquisition settings, and primary reduction equations

Test	Standard	Key dimensions	Acquisition settings	Primary equations used
Tensile	ASTM E8	Total length of 100 mm; gauge length of 25 mm; gauge width of 6 mm; shoulder width of 10 mm; thickness of 2 mm	UTM of 100 kN; crosshead of 1 mm min^{-1}; extensometer with a 25 mm gauge length; $n = 5$	$\sigma_e = F/A_0$; $\varepsilon_e = \Delta L/L0$; $\sigma = E(\varepsilon_e - 0.002)$; $\sigma UTS = \max(\sigma_e)$; $A\ (\%) = (Lf - L0)/L0 \times 100$; $U = \int \sigma_e d\varepsilon_e$
Hardness	Vickers	Indent diagonal, d, measured optically on specimens measuring	Multiple indents per specimen	$HV = 1.8544\ F/d^2$; $F = FN/9.80665$
Izod impact	ASTM D256	75 × 10 × 10 mm; V-notch depth of 2 mm; 45°; root radius of 0.25 mm	Pendulum capacity of 300 J; $n = 5$	$EI = E_0 - E_r$

from the final gauge length after fracture, Lf, and the initial gauge length, L_0, using $A\ (\%) = (Lf - L_0)/L_0 \times 100$. When tensile energy absorption was evaluated from the stress-strain record, the strain-energy density U was calculated by numerical integration up to the fracture strain, σf, using Equation (1):

$$U = \int_0^{\varepsilon_f} \sigma_e \, d\varepsilon_e \tag{1}$$

and discrete data were reduced using the trapezoidal approximation, i.e., Equation (2):

$$U = \sum_{i=1}^{N-1} \frac{\sigma_{e,i} + \sigma_{e,i+1}}{2} (\varepsilon_{e,i+1} - \sigma_{e,i}) \tag{2}$$

Five specimens were tested per condition, and replicate processing followed identical gripping practice and acquisition settings.

Vickers hardness was measured on polished specimen surfaces and was recorded in HV. Multiple indents were placed on each specimen, with spacing selected to prevent overlap of plastic zones, and condition values were obtained from replicate measurements. Hardness was computed from the applied load and indentation geometry using the standard Vickers relation $HV = 1.8544\ F/d^2$, in which F denotes the applied load in kgf and d denotes the mean diagonal length in mm. When the applied load was recorded in newtons (F_n), the conversion $F = F_n/9.80665$ was applied before substitution into the Vickers expression. The same polishing sequence and measurement protocol were applied to all conditions to limit surface-finish effects on diagonal measurement.

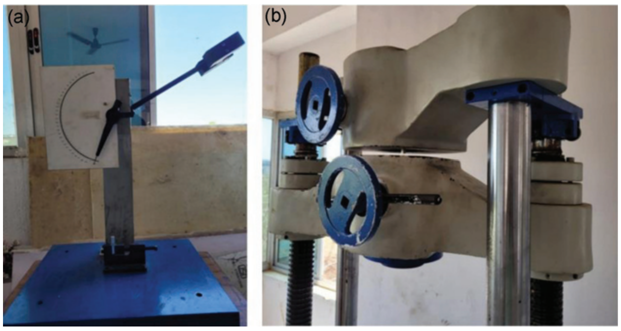

Figure 4: Izod impact test setup

Table 6: Metallography, microscopy, and image-based quantification parameters and equations

Workflow element	Parameter	Value/method	Quantities computed
Mounting	Mount medium	Bakelite	—
Grinding	Abrasive sequence	320–2000 grit SiC	—
Polishing	Diamond suspensions	6 µm and 1 µm	—
Etching	Reagent and time	Keller's reagent, 15–20 s	—
SEM	Operating conditions	15 kV; working distance of near 10 mm	EDS spot spectra; elemental maps
Area fraction	Segmentation + check	Threshold segmentation; point counting check	$A_A = A_p/A_T$; $A_A = P_p/P_T$
Particle size	Size descriptor	Equivalent-circle diameter	$d_{eq} = 2\sqrt{(A / \pi)}$
Free path	Line-intercept sampling	Test lines on binarised maps	$\lambda = (LT - \Sigma l_p)/N_g$
Statistics	Summary descriptors	Replicate aggregation	$\bar{x}$; s; ΔX (%)
Modelling	Regression/ANOVA/RSM	Linear and quadratic forms	R^2; F; desirability d(y) and D

Izod impact testing was conducted using a pendulum impact tester with a 300 J hammer capacity. A specimen was mounted vertically with the notch facing the striker, and the absorbed energy was read from the calibrated machine scale after fracture. The impact configuration and specimen placement are shown in **Figure 4**, and the corresponding specimen dimensions are listed in **Table 6**. When the initial and residual pendulum energies were obtained from the instrument records, absorbed energy, EI, was computed as $EI = E_0 - E_r$, where E_0 denotes the initial potential energy, and E denotes the residual energy after fracture. Five specimens were tested per condition, and identical notch orientation relative to the striker was maintained across tests to standardize the local stress state at the notch root.

Microstructural and compositional characterization was performed using optical microscopy and scanning electron microscopy coupled with energy-dispersive spectroscopy. Samples were extracted from cast bars, mounted in bakelite, and ground using SiC papers from 320 to 2000 grit under water lubrication, followed by diamond polishing with 6 µm and 1 µm suspensions. Keller's reagent was applied for 15–20 s to reveal matrix features and reinforcement distribution, followed by rinsing and drying. SEM observations were conducted at 15 kV and a working distance of approximately 10 mm, and EDS spot analysis and mapping were used to verify reinforcement-associated elemental signals. Quantitative microstructural descriptors were obtained from polished sections using image segmentation and stereological calculations. Particle area fraction was computed as $A_a = A_p/A_t$, where A_p denotes segmented particle area, and A_t denotes total field area. The point-counting estimate was treated as $A_a = P_p/P_t$, where P_p denotes particle hits, and P_t denotes total points. Particle size was represented using an equivalent-circle diameter calculated from segmented particle area A as $d_e q = 2\#(A/\pi)$. Mean matrix free path was computed from line-intercept sampling using $\lambda = (L_t - \Sigma l_p)/N_g$, where L_t denotes total test-line length, Σl_p denotes the summed chord length through particles, and N_g denotes the number of matrix gaps intercepted. The imaging, preparation, and quantification parameters used for microscopy and image analysis are listed in **Table 5**. Identical preparation and analysis settings were applied across all conditions to limit operator-induced variation.

3 RESULTS AND DISCUSSSION

Figure 5 illustrates the fracture morphology of the AA7065–B_4C–graphite hybrid under tensile loading, linking micro-scale damage features with the macroscopic strength and ductility behaviour that was measured earlier. **Figure 5a** shows closely packed tear ridges and fine secondary steps oriented along the tensile loading direction, together with fractured angular particles and small cavities, so the fracture path is guided by intense plastic shearing of the aluminium matrix around stiff B_4C inclusions. The tests showed higher yield and ultimate strengths for reinforced specimens, and these elongated ridges indicate that dislocation glide was strongly constrained and channelled along narrow bands before the final separation.[25] **Figure 5b** shows a broader, 100 µm field where thick, plate-like shear regions surround a central depressed zone, with scattered bright particles decorating the surface. The fracture process therefore involved macroscopic shear localization and necking, followed by rapid crack advance through regions where reinforcement density was high.[26] **Figure 5c** shows a large cavity bounded by a relatively smooth basin and surrounded by jagged ligaments studded with bright fragments, corresponding to the pull-out of a B_4C or graphite-rich cluster. The experiment thus revealed that debonding at the particle-matrix interface occurred once local stresses exceeded the interfacial strength, and subsequent microvoid coalescence produced sizeable pores that weakened the remaining load-bearing cross-section.[27] **Figure 5d** shows an extensive rough surface with numerous small dimples, multiple clustered particles and narrow valleys linking neighbouring cavities, indicating mixed-mode failure where ductile microvoid growth in matrix ligaments interacts with brittle cracking inside or around ceramic particles. This

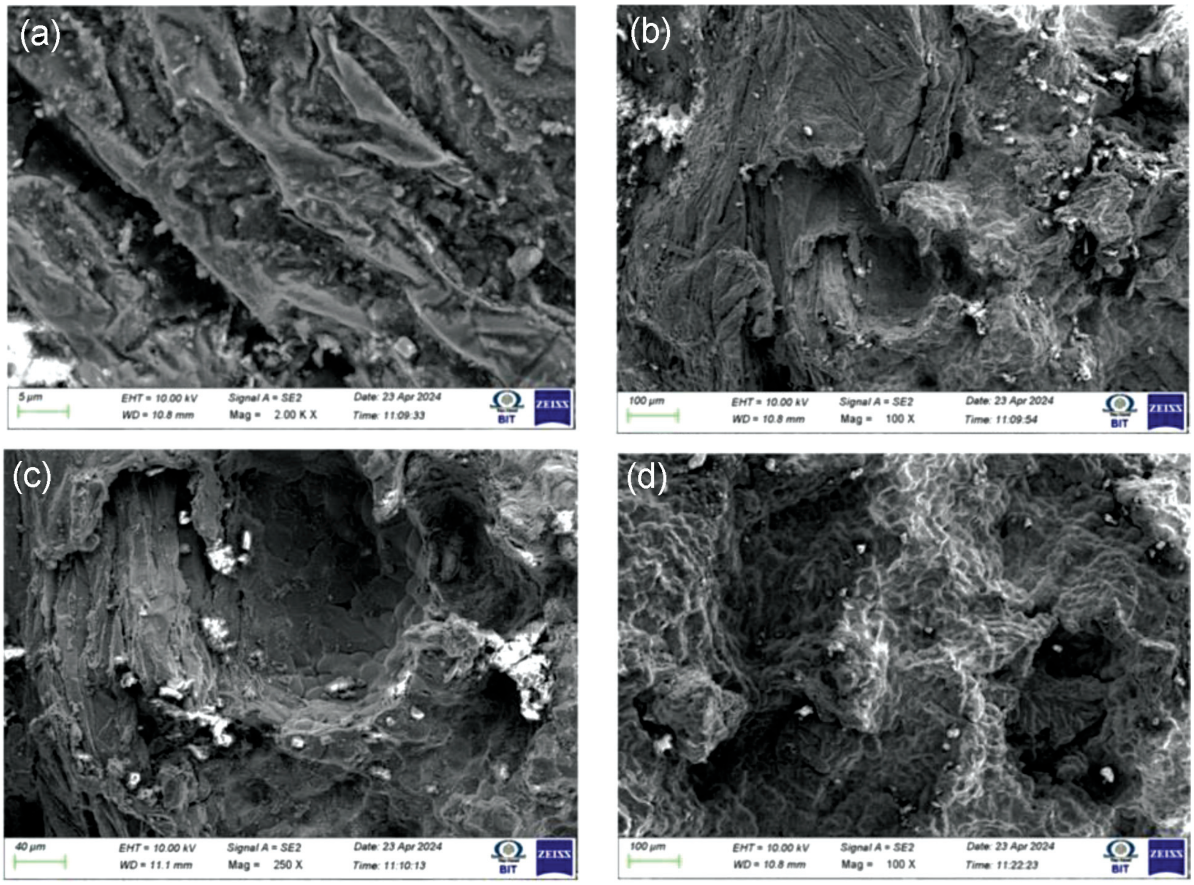

Figure 5: a) High-magnification SEM fracture surface of AA7065–B_4C–graphite hybrid composite; b) low-magnification view revealing large shear facets; c) intermediate-magnification image; d) SEM overview displaying mixed-mode fracture

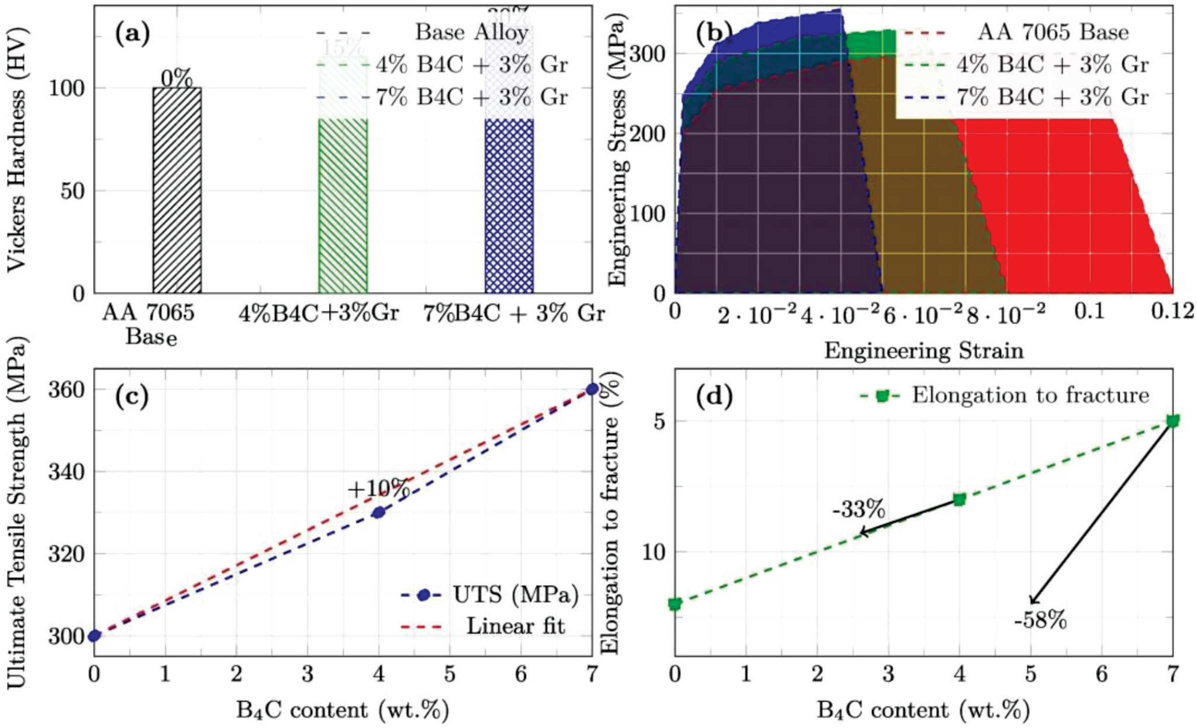

Figure 6: a) Vickers hardness of AA7065 base alloy and AA7065–B_4C–3 *w*/% graphite composites; b) engineering stress–strain curves for AA7065 base alloy and hybrids with 4 and 7 *w*/% B_4C; c) ultimate tensile strength as a function of B_4C content at constant 3 *w*/% graphite; d) elongation to fracture versus B_4C content at constant 3 *w*/% graphite

morphology is consistent with the recorded reduction in elongation to fracture for higher B_4C contents, and with the moderate energy absorption capacity of the hybrids. These fracture features suggest that B_4C additions increase constraint and promote higher stress triaxiality ahead of the crack tip, while graphite inclusions assist crack deflection and local sliding. As a result, the composite exhibits enhanced strength but a stronger tendency for early void nucleation and accelerated crack propagation, which is important for designing AA7065-based components where reliable damage tolerance under static loading is required.[28]

Figure 6 presents the comparative behaviour of the AA7065 base alloy and B_4C–graphite-reinforced hybrids under quasi-static loading, linking hardness, strength, and ductility coherently. **Figure 6a** shows that the Vickers hardness increases from about 100 HV for the base alloy to roughly 115 HV for the 4 *w*/% B_4C + 3 *w*/% Gr composite and nearly 130 HV for the 7 *w*/% B_4C + 3 *w*/% Gr composite, indicating gains of about 15 % and 30 %, respectively. These increments arise because stiff B_4C particles constrain local plastic flow and elevate dislocation density, while graphite at a fixed content contributes negligibly to indentation resistance.[29] **Figure 6b** shows that the engineering stress–strain curve of the base alloy exhibits a 0.2 % proof stress of around 200 MPa, a UTS near 300 MPa and a fracture strain close to 0.12; the 4 *w*/% B_4C hybrid displays a higher yield stress of about 220–230 MPa and a UTS of ≈340 MPa, with a fracture strain near 0.06; the 7 *w*/% B_4C hybrid reached ≈250 MPa yield stress and ≈360 MPa UTS, with a strain to failure near 0.04–0.05. The shaded areas indicate that the base alloy absorbed the largest tensile energy, while the more heavily reinforced composites failed at a lower strain despite higher peak stresses; this behaviour reflects early void nucleation at particle–matrix interfaces and rapid microvoid coalescence once the matrix is locally exhausted of plasticity.[30] **Figure 6c** shows that the UTS rises almost linearly from about 300 MPa at 0 *w*/% B_4C to roughly 330 MPa at 4 *w*/%, and 360 MPa at 7 *w*/%, implying an effective strengthening rate of around 8–9 MPa per *w*/% B_4C and suggesting that dispersion quality remains adequate up to the highest ceramic level examined.[31] Figure 6d shows a nearly linear decline in elongation from about 12 % for the base alloy to roughly 8 % and 5 % at (4 and 7) *w*/% B_4C, corresponding to ductility reductions of ≈33 % and ≈58 %; such behaviour is characteristic of particulate-reinforced aluminium matrix composites where increasing ceramic fraction reduces the volume of contiguous ductile ligaments and intensifies stress concentrations.[32]

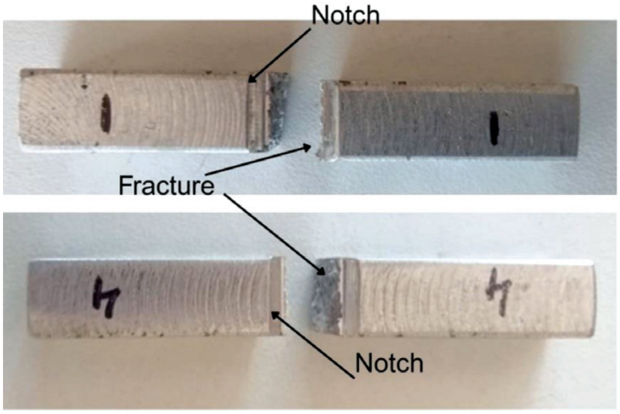

Figure 7: Izod impact test fractured specimens

Figure 7 shows macrophotographs of fractured Izod impact test specimens, illustrating the deformation regions, notch locations, and fracture faces for the AA 7065 base alloy and its hybrid composites. The base alloy specimen displays a more pronounced plastic deformation zone adjacent to the notch, evidenced by smoother and more elongated shear lips along the fracture surface. This reflects the alloy's higher ductility and capacity to undergo stable plastic flow before complete separation. In contrast, the hybrid composite specimens, particularly those with a higher B_4C content, exhibit reduced notch-root deformation and sharper, more granular fracture surfaces, indicative of brittle behaviour.[33] The reduced plastic zone size in the composites aligns with the lower impact energy absorption values measured during testing, where reinforcement particles act as crack initiation points and promote rapid crack propagation. The 4% B_4C + 3% graphite specimen shows a limited shear lip formation, with its depth and width smaller than for the base alloy, consistent with its 20 % lower impact energy. The 7 % B_4C + 3% graphite specimen shows the most abrupt fracture path with minimal necking or shear deformation, correlating with a 40 % reduction in absorbed energy.[34] The observed fracture features underscore the influence of reinforcement content on toughness, with an increasing ceramic fraction suppressing ductile tearing and shifting fracture modes toward brittle cleavage and particle-assisted crack growth. These macro features provide qualitative validation of the quantitative impact energy trends and reinforce the microstructural mechanisms governing fracture in particle-reinforced aluminium composites.

4 CONCLUSIONS

This study investigated stir-cast AA7065–B_4C–graphite hybrid metal–matrix composites to examine the relationships among reinforcement content, microstructure, and mechanical response after precipitation hardening. Hybrids were produced by vortex-assisted stir casting, followed by a T6 schedule, machined into ASTM E8 and ASTM D256 specimens, tested for hardness, tension, and Izod impact, and examined by optical microscopy and SEM/EDS, supported by regression-based ANOVA and response-surface optimisation. Introducing 4 *w*/% B_4C with 3 *w*/% graphite increased hardness by 16.7 % and tensile strength by 12.0 %, while impact toughness decreased by 20 %. At 7 *w*/% B_4C, the corresponding changes reached 33.3 % and 22.0 %, and impact toughness decreased by 40 %. Hardness–impact correlations indicated that at 120 HV the base alloy fractured at a higher absorbed energy than the 4 *w*/% B_4C hybrid at 140 HV, which absorbed 16 J. The 7 *w*/% B_4C hybrid reached 160 HV under testing. Response-surface optimisation yielded an increase in yield strength from 458.3 MPa to 606.7 MPa and in ultimate tensile strength from 515.4 MPa to 683.6 MPa, with a desirability index of 0.825 at 7 *w*/% B_4C and 2 *w*/% graphite. Fractography revealed particle cracking, pull-out, and microvoid coalescence, consistent with reinforcement-assisted void nucleation and reduced plastic deformation before separation. These outcomes provide a quantitative basis for selecting reinforcement levels for AA7065 hybrids used in structural and tribological components, where strength elevation must be balanced with impact resistance. Future investigations will quantify fatigue and wear response, examine graphite fraction and particle-size distributions beyond the present design space, and integrate micromechanical modelling with process-structure calibration.

Acknowledgments

Conflict of Interest Statement:

The author(s) declared no potential conflicts of interest.

Funding Declaration:

No financial support was provided.

Data Availability

The datasets used during the current study are available from the corresponding author on reasonable request.

5 REFERENCES

[1] K. Shivalingaiah, N. Vinayaka, C. P. Pon Selvan, S. T. Kariappa, N. G. Chandrashekarappa, A. Avinash, et al., Stir Casting Process Analysis and Optimization for Better Properties in Al-MWCNT-GR-Based Hybrid Composites, Metals (Basel), 12 (**2022**), doi:10.3390/met12081297

[2] D. V. Devu, P. S. Sravani, N. Deepthi, C. Thirupathaiah, The investigation of mechanical and metallurgical properties on Al7075-TiC-SiC reinforced hybrid composites by stir casting, International Journal of Mechanical and Production Engineering Research and Development, 9 (**2019**), 769–76, doi:10.24247/IJMPERDAPR201976

[3] L. Tharanikumar, B. Mohan, G. Anbuchezhiyan, Enhancing the microstructure and mechanical properties of Si3N4-BN strengthened Al-Zn-Mg alloy hybrid nano composites using vacuum assisted stir casting method, Journal of Materials Research and Technology, 20 (**2022**), 3646–55, doi:10.1016/j.jmrt.2022.08.093

[4] M. Manickaraj, M. Marimuthu, S. Rajesh, M. S. Abdul Majid, S. Rajakarunakaran, M. Niemczewska-Wójcik, Dry Sliding Wear Studies on Sillimanite and B4C Reinforced Aluminium Hybrid Composites Fabricated by Vacuum Assisted Stir Casting Process, Materials, 16 (**2023**), doi:10.3390/ma16010259

[5] D. Ren, C. Wang, X. Wei, Y. Zhang, S. Han, W. Xu, Harmonizing physical and deep learning modeling: A computationally efficient and interpretable approach for property prediction, Scr. Mater., 255 (**2025**), 116350, doi:10.1016/j.scriptamat.2024.116350

[6] C. Wang, Z. Zhang, X. Jing, Z. Yang, W. Xu, Optimization of multi-stage femtosecond laser drilling process using machine learning coupled with molecular dynamics, Opt. Laser Technol., 156 (**2022**), 108442, doi:10.1016/j.optlastec.2022.108442

[7] Z. Zhang, S. Liu, Y. Zhang, C. Wang, S. Zhang, Z. Yang, et al., Optimization of low-power femtosecond laser trepan drilling by machine learning and a high-throughput multi-objective genetic algorithm, Opt. Laser Technol., 148 (**2022**), 107688, doi:10.1016/j.optlastec.2021.107688

[8] H. Xu, D. Geng, X. Jiang, J. Xue, G. Guo, D. Zhang, An innovative normal self-positioning method with gravity and friction compensation for wall-climbing drilling robot in aircraft assembly, The International Journal of Advanced Manufacturing Technology, 138 (**2025**), 3687–704, doi:10.1007/s00170-025-15677-7

[9] K. Zheng, Z. Min, F. Zhang, Z. Ren, Y. Lin, High heat-fade resistance, metal-free resin-based brake pads: A step towards replacing copper by using andalusite, Chinese Journal of Mechanical Engineering, 38 (**2025**), 153, doi:10.1186/s10033-025-01310-x

[10] C. Xiao, J. Peng, Y. Jiao, Q. Shen, Y. Zhao, Q. Song, Strong and tough multilayer heterogeneous pyrocarbon based composites, Adv. Funct. Mater., 34 (**2024**), 2409881, doi:10.1002/adfm.202409881

[11] X. Cheng, J. Hu, A. Wan, X. Ji, Optimizing Inconel 718 micro-hole drilling using response surface and random forest methods, Measurement, 262 (**2026**), 120032, doi:10.1016/j.measurement.2025.120032

[12] P. Ma, H. Yang, Z. Zhang, X. Xie, Y. Jia, Microstructure and mechanical properties of additively manufactured FeCoCrMnNi high-entropy alloy composite after aging, J. Cent. South Univ., 32 (**2025**), 1167–78, doi:10.1007/s11771-025-5929-z

[13] X. Meng, W. Wang, Y. Huang, Microstructural modification and stress corrosion mechanisms of in-situ rolling friction stir welding joints, Mater. Charact., 231 (**2026**), 115884, doi:10.1016/j.matchar.2025.115884

[14] J. Peng, S. Xie, T. Chen, Z. Yang, Numerical simulation and process optimization of laser welding in 6056 aluminum alloy T-joints, Crystals (Basel), 15 (**2025**), 35, doi:10.3390/cryst15010035

[15] Q. Qiao, L. Wang, C. W. Tam, X. Gong, Y. Lin, In-situ monitoring of additive friction stir deposition of AA6061: Effect of rotation speed on the microstructure and mechanical properties, Materials Science and Engineering A, 902 (**2024**), 146620, doi:10.1016/j.msea.2024.146620

[16] F. Yuan, Y. Han, K. Xiao, G. Xiang, Z. Wang, X. Chen, Spatial modification optimization methods for harmonic drives using a 3D non-uniform line-contact elastohydrodynamic lubrication model, Tribol. Int., (**2025**), 111288, doi:10.1016/j.triboint.2025.111288

[17] K. Zheng, Q. Le, L. Pan, J. Huang, Friction and wear prediction of copper-free resin-based brake materials: A hybrid PSO-FPA-BP neural network approach, Wear, 589 (**2026**), 206536, doi:10.1016/j.wear.2026.206536

[18] S. Nanjan, G. M. Janakiram, Characteristics of A6061/(Glass Fibre + AL2O3 + SiC + B4C) Reinforced Hybrid Composite Prepared through STIR Casting, Advances in Materials Science and Engineering, (2019), doi:10.1155/2019/6104049

[19] C. R. Ramesh Kannan, S. Suresh, M. N. Navaneetha Krishnan, Influence of acustic emission signals and damage analysis during the tensile test on Al8011 hybrid composites by stir casting method, Archives of Metallurgy and Materials, 68 (**2023**), 223–35, doi:10.24425/amm.2023.141498

[20] S. P. Dwivedi, G. Dwivedi, Utilization of RHA in development of hybrid composite by electromagnetic stir casting technique using RSM, Journal of Metals, Materials and Minerals, 29 (**2019**), 45–54, doi:10.55713/jmmm.v29i4.538

[21] S. Senthil Murugan, M. Vigneshkumar, M. John Iruthaya Raj, S. Selvaraju, N. Vinayaka, S. Srinivasan, et al., Stir Casting Processing, Mechanical, and Wear Behavior of AA2024 + 10 wt. % Flyash + 5

wt. % Graphite Hybrid Composite, Advances in Materials Science and Engineering, (2023), doi:10.1155/2023/9089620

[22] S. Raja, V. Veerabathiran, Mechanical and wear characteristics of (Al7075/SiC/Gr/Zr) hybrid metal matrix composites using ultrasonic assisted stir casting process, International Journal of Advanced Technology and Engineering Exploration, 10 (**2023**), 660–75, doi:10.19101/IJATEE.2021.876468

[23] S. R. Hariharan, S. Sakthi, S. Mahendran, S.T. Jayasuthakar, Influence of MgO & SiC on mechanical and wear characteristics of AA6061 hybrid matrix composites synthesized by stir casting, Journal of Applied Research and Technology, 21 (**2023**), 162–8, doi:10.22201/icat.24486736E.2023.21.2.1618

[24] M. K. Kumar Singh, R. K. Gautam, G. Ji, Mechanical properties and corrosion behavior of copper based hybrid composites synthesized by stir casting, Results Phys., 13 (**2019**), doi:10.1016/j.rinp.2019.102319

[25] G. Zhang, J. Gu, H. Shi, P. Zhang, G. Yang, Microstructures and mechanical properties analysis of TiAl joints using novel brazing filler metal, Welding in the World, (2025), doi:10.1007/s40194-025-02210-3

[26] C. Zhang, M. Lou, Y. Wang, T. Sui, Mechanical responses and microscopic irreversible deformation evolution of thermoplastic fiber-reinforced composites under cyclic loading, Int. J. Fatigue, 203 (**2026**), 109327, doi:10.1016/j.ijfatigue.2025.109327

[27] S. Kaliappan, A. Shanmugam, P. Johnson, M. Karthick, S. Sekar, PP Patil, et al., Impact of AlN-SiC Nanoparticle Reinforcement on the Mechanical Behavior of Al 6061-Based Hybrid Composite Developed by the Stir Casting Route, Advances in Materials Science and Engineering, (2022), doi:10.1155/2022/1399618

[28] P. Gnaneswaran, V. Hariharan, S. J. S. Chelladurai, G. Rajeshkumar, S. Gnanasekaran, S. Sivananthan, et al., Investigation on Mechanical and Wear Behaviors of LM6 Aluminium Alloy-Based Hybrid Metal Matrix Composites Using Stir Casting Process, Advances in Materials Science and Engineering, (2022), doi:10.1155/2022/4116843

[29] L. Zhang, H. Zhang, Ti-based metallic glass composites containing β-Ti dendrites, Prog. Mater. Sci., 152 (**2025**), 101472, doi:10.1016/j.pmatsci.2025.101472

[30] B. Gugulothu, P. Peyyala, M. N. Nagaswapnasri, S. S. Vijayakumar, R. Periyasamy, S. Seetharaman, Optimization of Stir-Squeeze Casting Parameters to Analyze the Mechanical Properties of Al7475/B4C/Al2O3/TiB2 Hybrid Composites by the Taguchi Method, Advances in Materials Science and Engineering, (2022), doi:10.1155/2022/3180442

[31] Y. Zhang, Z. Zhang, J. Sun, Machine learning guided design and ablation behavior of ZrC-TaC-SiC ternary coatings, Corros. Sci., 260 (**2026**), 113499, doi:10.1016/j.corsci.2025.113499

[32] C. Duan, L. Guan, R. Zhang, Rapid microwave heating synthesis and microwave coupling mechanism of transition metal high-entropy carbides, Ceram. Int., 51 (**2025**), 47506–15, doi:10.1016/j.ceramint.2025.08.308

[33] S. Suresh Pungaiah, K. K. Sahu, R. Yuvaraja, G. Prabhu, R. Raja Sudharsan, P. Thamizhvalavan, et al., Investigation on Mechanical Behaviour of LM6 Aluminum Alloy Hybrid Composites Processed Using Stir Casting Process, Advances in Materials Science and Engineering, (2022), doi:10.1155/2022/7539546

[34] X. Zhang, J. Sun, Y. Zhang, Machine learning for phase prediction of high entropy carbide ceramics from imbalanced data, NPJ Comput. Mater., (2026), doi:10.1038/s41524-025-01873-2